IRS-Assisted Hyperspectral Image Processing in Satellite Edge Computing Services

Xiaoteng Yang, Jie Feng, *Member, IEEE*, Lei Liu, *Member, IEEE*, Qingqi Pei, *Senior Member, IEEE*, Shahid Mumtaz, *Senior Member, IEEE*, Keqin Li, *Fellow, IEEE*, and Schahram Dustdar, *Fellow, IEEE*

***Abstract*—The rapid development of satellite technology has significantly enhanced satellite computing service capabilities, particularly in terms of its application potential for complex tasks such as hyperspectral image (HSI) processing. Satellite edge computing (SEC) substantially improves processing efficiency by transferring task processing to the satellite. At the same time, intelligent reflective surfaces (IRS) reduce the pressure on ground service center communication resources by optimizing communication links between satellites on the ground. However, existing works mainly optimize general computing tasks, resulting in limited performance when processing HSI tasks. This paper proposes an IRS-assisted HSI processing SEC system to achieve the optimal balance between HSI processing accuracy and system energy consumption. We formulate an optimization problem as a joint task covering HSI offloading, band selection, and IRS phase shift optimization to achieve optimal overall performance. To address the problem, we propose the joint feature iterative optimization (JFIO) framework for HSI processing, which generates optimized task offloading solutions through graph attention networks, utilizes multi-feature attention capsule networks to achieve efficient band selection, and combines this with IRS modules to optimize communication link conditions. Extensive experiments on various datasets demonstrate that the proposed framework achieves an excellent balance between accuracy and energy consumption, with its performance significantly outperforming other baseline methods.**

***Index Terms*—Band selection, hyperspectral image processing, intelligent reflective surface, satellite edge computing, task offloading.**

Received 28 March 2025; revised 22 July 2025; accepted 24 July 2025. Date of publication 4 August 2025; date of current version 9 October 2025. This work was supported in part by the National Natural Science Foundation of China under Grant U24A20241 and Grant 62132013, in part by the Key Research and Development Programs of Shaanxi under Grant 2024GX-YBXM-071 and Grant 2025SYS-SYSZD-080, in part by Basic Strengthening Plan Program under Grant 2023-JCJQ-JJ-0772, in part by the Fundamental Research Funds for the Central Universities under Grant QTZX25085, in part by Guangdong Basic and Applied Basic Research Foundation 2025A1515012741, in part by the Key Laboratory of Computing Power Network and Information Security, Ministry of Education under Grant 2023ZD008, in part by the Innovation Fund of Xidian University, and in part by China Scholarship Council. *(Corresponding authors: Jie Feng; Qingqi Pei.)*

Xiaoteng Yang and Jie Feng are with the School of Telecommunications Engineering, Xidian University, Xi'an 710071, China (e-mail: xtengyang@stu.xidian.edu.cn; jiefengcl@163.com).

Lei Liu is with the Guangzhou Institute of Technology, Xidian University, Guangzhou 510555, China, and also with the Key Laboratory of Computing Power Network and Information Security, Ministry of Education, Qilu University of Technology(Shandong Academy of Sciences), Jinan 250014, China (e-mail: leiliu@xidian.edu.cn).

Qingqi Pei is with the State Key Laboratory of Integrated Services Network, the Shaanxi Key Laboratory of Blockchain and Secure Computing, Xidian University, Xi'an 710071, China (e-mail: qqpei@mail.xidian.edu.cn).

Shahid Mumtaz is with the Department of Computer Sciences, Nottingham Trent University, NG1 4FQ Nottingham, U.K., and also with the Department of Electronic Engineering, Kyung Hee University, Yongin-si 17104, South Korea (e-mail: dr.shahid.mumtaz@ieee.org).

Keqin Li is with the Department of Computer Science, State University of New York, New York, NY 12561 USA (e-mail: lik@newpaltz.edu).

Schahram Dustdar is with the Distributed Systems Group, TU Wien, 1040 Vienna, Austria (e-mail: dustdar@dsg.tuwien.ac.at).

Digital Object Identifier 10.1109/TSC.2025.3595166

I. Introduction

A. Background and Motivation

With the rapid development of satellite computing, low Earth orbit (LEO) satellites have become key players in communications, navigation, meteorology, and environmental monitoring. The number of LEO satellites is projected to reach 12,000 by 2027 [1], [2], [3], [4], [5], [6], with nearly half dedicated to Earth observation. Hyperspectral imaging (HSI), in particular, is widely used in agriculture, ecology, and environmental monitoring due to its ability to capture fine-grained spectral information. However, the surge in data volume has outpaced improvements in onboard processing and transmission, causing congestion and delays [7], [8], [9], [10]. Each satellite generates large volumes of high-resolution HSI data, yet typically communicates with ground stations only 3–5 times per day, with a maximum transmission rate of 7.5 Mbps. This mismatch between data generation and downlink capacity leads to backlogs and limits real-time responsiveness. Energy and bandwidth constraints further hinder timely data delivery [11], [12], [13], [14].

To address the challenges of limited communication bandwidth and energy resources and to meet the demand for efficient data processing and real-time response services, satellite edge computing (SEC) has emerged as a key research direction. Modern satellites serve as relays and undertake onboard data processing tasks [15], [16], [17], [18], [19]. For example, SpaceX's Starlink constellation is already in the public testing phase, while Lumen Orbit is about to launch satellites equipped with GPUs to enable real-time data processing. Although in-orbit HSI processing offers significant advantages in data efficiency and real-time performance, it also introduces challenges not present in ground-based processing, such as limited computational resources, strict power constraints, and thermal management issues [20], [21], [22]. The massive amount of data generated by hyperspectral imagers requires powerful processing capabilities, so optimizing the use of computational resources under limited satellite space and power consumption is crucial.

Currently, SEC research focuses on single satellite processing tasks without considering task distribution to neighboring satellites. Researchers have proposed various approaches to address this problem. Song et al. developed energy-efficient computation offloading and resource allocation algorithms using fractional planning and Lagrangian dyadic methods [23]. Mei et al. combined high-altitude platforms and satellites to provide computation services on the ground and optimize energy consumption through intelligent algorithms [24]. Sthapit et al. used deep reinforcement learning to comprehensively consider the energy consumption, latency, and cost in order to maximize the performance of the system [25]. Li et al. focused on the battery sensing energy optimization and proposed an online energy scheduling algorithm to extend battery life [26]. However, existing studies mostly focus on isolated satellite processing, overlooking the potential benefits of multi-satellite collaborative computing. The lack of cooperative strategies leads to resource underutilization, especially when one satellite is overloaded while others remain underused. Multi-satellite cooperative computing through inter-satellite links (ISL) can significantly enhance resource utilization and load balancing. Mayorga et al. constructed a real-time earth observation framework by distributing data through ISL and optimized image distribution to reduce energy consumption [27]. Zhang et al. proposed a multi-hop peer offloading scheme to reduce system latency and energy consumption [28]. Wu et al. solved the offloading problem in task migration based on the dueling double deep Q network (D3QN) algorithm to minimize system latency [29]. Cui et al. performed LEO and geostationary earth orbit satellites for communication and computational resource optimization [30]. Tang et al. established a dual time-scale hierarchical framework to optimize the satellite network and QoS [31]. While these studies highlight the potential of SEC, they do not sufficiently address the specific challenges of HSI data processing and the unique characteristics of satellite networks, such as limited contact windows and dynamic resource availability.

HSIs contain rich band information and typically require dimensionality reduction, such as band selection, before transmission to retain essential semantic and spectral features. Implementing band selection at the satellite side is crucial to alleviate data transmission pressure and enhance the efficiency of onboard processing. With the development of SEC technology, transferring these preprocessing operations to the satellite side is essential. This enables the satellite to prioritize the information-rich bands within a limited contact window and thus transmit more hyperspectral data. Cai et al. applied graph convolutional networks to the band selection model, significantly improving the performance of traditional methods [32]. Li et al. proposed a representative band selection method in a local context by fitting spectral curves and efficiently identifying the desired bands through sorting and iterative updating [33]. In addition, Zhu et al. proposed a two-layer collaborative processing framework MaHSI, which treats frequency selection as a utility problem and considers energy, communication, and delay factors to achieve good accuracy and inference speed [4].

Although processing at the satellite end improves data transmission efficiency, satellite-to-ground communication still suffers from signal attenuation, propagation delay, and transmission instability, especially in dynamic orbital environments [34], [35]. Therefore, introducing intelligent reflective surface (IRS) technology is critical, as it significantly improves communication between satellites and ground service centers by optimizing the reflection and transmission paths of signals. Studies have shown that precise manipulation of the reflective elements in IRS can optimize signal strength and improve wireless communication capabilities and transmission speed. For example, Zheng et al. proposed an IRS-based low-orbit satellite communication architecture that significantly reduces signal attenuation [36]. Liu et al. introduced IRS phase shift vectors and proposed a low-complexity beam fouling algorithm to ensure the quality of service [37]. Shaik et al. combined airborne and ground-based IRS nodes to perform a comprehensive performance analysis of a satellite network, aiming to maximize spectral efficiency [38].

However, traditional HSI band selection methods do not adequately address the complex dynamic constraints of satellite edge networks. These methods often assume stable links and abundant computing resources, which are impractical in dynamic satellite environments. Therefore, it is imperative to propose novel methods tailored to hyperspectral imaging and satellite edge computing challenges.

B. Solution Approach and Contributions

This work proposes an IRS-assisted SEC system for optimized HSI processing, where collaboration between satellites and the ground service center enhances data transmission and processing efficiency. The system consists of a local LEO satellite and multiple neighboring satellites equipped with edge computing systems to process HSI. The IRS significantly empowers satellites by precise phase control of reflective elements. In particular, IRS enables dynamic adaptation to environmental conditions, maintaining robust communication between satellites and the ground service center. Unlike traditional methods that optimize only one aspect of satellite edge computing, we propose a novel joint feature iterative optimization (JFIO) framework, which jointly optimizes task offloading, HSI band selection, and IRS phase control to maximize system efficiency. JFIO does not treat these components separately; instead, it dynamically integrates them, ensuring adaptability to changing satellite network conditions. Through continuous feedback loops among task allocation, feature selection, and communication enhancement, JFIO achieves synergistic improvements in processing performance, energy efficiency, and communication quality.

At the core of JFIO, a graph attention network (GAT) is employed to generate task offloading scenarios based on satellite resource availability, followed by a multi-feature attention capsule network (MACN) for selecting the most informative bands. While GAT has been applied in various domains, its role here is not an independent innovation but an essential component within the iterative optimization process. The outputs of GAT and MACN further guide the IRS phase optimization module, adjusting channel conditions to improve communication quality.

These interconnected modules form a dynamic feedback loop, ensuring continuous adaptation to network states and improving system flexibility and resource utilization. The main contributions are summarized as follows:

- We propose the JFIO framework, which optimizes task offloading, hyperspectral band selection, and IRS phase shift adjustment together, achieving superior system performance.
- We formulate an optimization problem to achieve an optimal trade-off between task processing accuracy and system energy consumption in the SEC system by integrating HSI task offloading, band selection, and IRS phase shift optimization.
- The formulated problem is a mixed-integer nonlinear programming (MINLP) problem. To reduce the problem's computational complexity, we present the JFIO framework, which iteratively refines its decision-making by leveraging the interdependencies among task allocation, feature selection, and communication enhancement rather than treating them as independent processes.
- Extensive experiments on real datasets show that the proposed framework achieves an excellent balance between task accuracy and energy consumption, and its performance significantly outperforms other baseline methods.

The rest of this paper is organized as follows. We first introduce the proposed system model and formulate the utility maximization problem in Section II. Section III describes the proposed JFIO framework. Section V introduces the experimental setup. Section IV analyzes the experimental results. Finally, Section VI concludes this paper.

II. System Model and Problem Formulation

In this section, we first describe the proposed SEC system and show the operation of the SEC system. Following this, we provide a detailed description of the coverage time model, the computing model, and the communication model. Finally, we formulate the optimization problem aimed at maximizing the overall utility of the system.

A. The Proposed SEC System

Fig. 1 represents our IRS-assisted HSI processing SEC system. First, an HSI feature classification model is trained on the ground and deployed on an airborne edge computing system. A LEO satellite in the system, called the local satellite, is equipped with a hyperspectral imager to capture HSI. It is surrounded by $M-1$ neighboring satellites, all of which are denoted as $\mathcal{M}=\{1,2,\ldots,M\}$, where 1 is the local satellite. Each satellite carries an onboard edge computing system for band selection and a communication system for HSI transmission. Meanwhile, the satellites are equipped with solar panels to harvest solar energy and deploy an IRS on the back of the satellite, which consists of K reflective primitives, denoted as $\mathcal{K}=\{1,2,\ldots,K\}$. The IRS is used to assist satellite communications by reconfiguring the wireless channel propagation through the precise adjustment of phase shifts across reflective elements, thereby improving the signal quality and transmission speed.

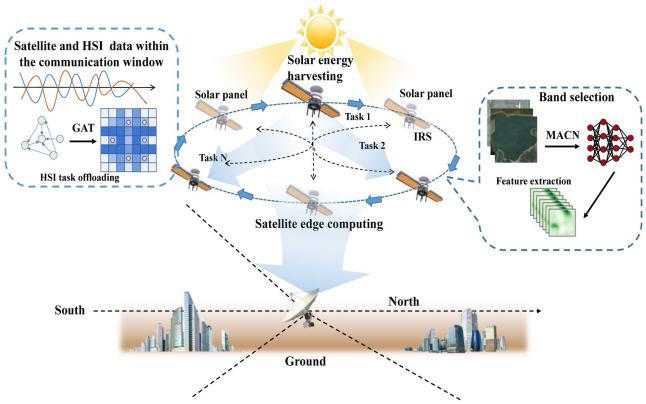

Fig. 1. The proposed IRS-assisted HSI processing SEC system.

TABLE I
Key Notations

Symbol	Description
$\mathcal{M}$	Set of all satellites, $\{1,\ldots,M\}$ (1: local)
$\mathcal{N}$	Set of HSI tasks, $\{1,\ldots,N\}$
$a_{n,m}$	Offloading decision: 1 if task n is assigned to satellite m
$x_{n,l}$	Band selection decision for band l in task n
ψ_k	Phase shift of the k-th IRS element
D_n	Data size of task n
C_n	Required CPU cycles for task n
$S_{m(n)}$	CPU frequency of satellite m for task n
$t^{comp}_{m(n)}$	Computation time of task n on satellite m
$E^{comp}_{m(n)}$	Computation energy for task n on satellite m
$t^{tran}_{1,m(n)}$	Transmission time from local to satellite m
$E^{tran}_{1,m(n)}$	Transmission energy
$t^{tran}_{m(n),g}$	Downlink transmission time to ground
$E^{tran}_{m(n),g}$	Downlink energy consumption
$R_{m,g}$	Downlink data rate from satellite m
A_n	Classification accuracy of task n
U_n	Utility of task n (performance vs. energy)
$T^{max}_{m(n)}$	Max contact duration of satellite m for task n

The system operates as follows: Before satellite launch, a band selector is trained on the ground using historical HSI data and deployed on the onboard edge computing system. After the satellite launches and reaches its orbit, the local satellite performs imaging and stores the captured HSI locally, denoted as $\mathcal{N}=\{1,2,\ldots,N\}$. The local satellite then assesses the availability of computing resources and the HSI content to determine an optimal offloading strategy. Based on this analysis, the local satellite transmits the HSI data or selected bands to neighboring satellites to maximize processing efficiency and balance computational load. During the contact window, the satellite transmits the selected frequency bands via downlink to the ground receiving station, where the data is further processed by the ground service center, depending on system conditions. The key notations used in the paper are listed in Table I.

B. Coverage Time Model

Unlike ground-based edge computing network, LEO satellites orbit the earth at lower altitudes, resulting in faster movement and larger orbital inclinations. Effective communication and

wide-area coverage can only be maintained when the relative position between the satellite and the ground service center is relatively fixed. The ground service center is located at the coordinates $l_g = (0, 0, 0)$, with R representing the earth's radius and $h_{m,g}$ denoting the height between the ground service center and the satellite's orbit. The arc length of the communication link between the satellite and the ground service center within the satellite's orbit is represented by $l_{m,g}$, while $s_{m,g}$ denotes the direct distance between the satellite and the ground service center. The satellite's position is given by the coordinates $l_m = (0, y_m, z_m)$. The distance $d_{m,g}$ from satellite m to the ground service center can be expressed as

$$d_{m,g} = \sqrt{R^2 + (R + h_{m,g})^2 - 2R(R + h_{m,g}) \cos \alpha_m}, \quad (1)$$

where α_m represents the azimuth angle of the satellite coverage, denoted as

$$\alpha_m = \arccos\left(\frac{R}{R + h_{m,g}} \cdot \cos \beta_m\right) - \beta_m, \quad (2)$$

where β_m represents the elevation angle between the ground service center and the satellite m, denoted as

$$\beta_m = \arccos\left(\frac{R + h_{m,g}}{d_{m,g}} \cdot \sin \alpha_m\right). \quad (3)$$

The communication arc length between satellite m and the ground service center is given by

$$l_{m,g} = 2 \cdot (R + h_{m,g}) \cdot \beta_m. \quad (4)$$

The maximum communication duration between satellite m and the ground service center while processing HSI n is

$$T^{max}_{m(n)} = \frac{l_{m,g}}{v_{m,n}}, \quad (5)$$

where $v_{m,n}$ represents the satellite's motion speed relative to the ground.

C. Computing Model

Next we present the computational model of the system, where the variable $a_{n,m} \in \{0, 1\}$ denotes the offloading decision. Specifically, $a_{n,m} = 1$ indicates that task n is offloaded for processing on satellite m, whereas $a_{n,m} = 0$ means the task is not assigned to that satellite. The content of different HSI tasks is $\Phi_n = \{D_n, C_n\}$, where D_n denotes the size of the task and C_n denotes the number of CPU cycles required to process the task. When the HSI is processed on satellite m, the band selector on the onboard edge computing system starts working. The computation time $t_{m(n)}$ for processing HSI on satellite m is

$$t^{comp}_{m(n)} = \frac{C_n \max\left\{1, \sum_{n \in \mathcal{N}} a_{n,m}\right\}}{S_{m(n)}}, \quad (6)$$

where $S_{m(n)}$ denotes the CPU clock speed at which satellite m processes HSI n. The term $\max\{1, \sum_{n \in \mathcal{N}} a_{n,m}\}$ models the workload of satellite m, ensuring that the computational latency dynamically adjusts based on the number of concurrent tasks being processed. Therefore the energy $E^{comp}_{m(n)}$ consumed for processing the HSI on the onboard edge computing system is given by

$$E^{comp}_{m(n)} = \sum_{m=1}^{M} t^{comp}_{m(n)} \cdot p_m \cdot \mathrm{I}\left[a_{n,m} = 1\right], \quad (7)$$

where p_m denotes the energy consumption of satellite m per CPU clock cycle, and $\mathrm{I}[a_{n,m} = 1]$ is an indicator function that takes a value of 1 if $a_{n,m} = 1$. After processing the HSI onboard the satellite, the selected bands are represented by the vector $\boldsymbol{x_n} = [x_{n,1}, x_{n,2}, \ldots, x_{n,l}]$, where $x_{n,l} \in \{0, 1\}$ and $l \in \{1, 2, \ldots, L\}$, with L being the total number of bands in the original HSI.

We use A to describe the performance of the transmitted HSI with respect to the analysis of the results of its selected bands, and the metric A_n denotes the overall accuracy of the different model treatments, i.e [4]

$$A_n = A(f_c(\boldsymbol{x_n}, d_n), \hat{y_n}), \quad (8)$$

where f_c denotes the different model classifiers, d_n denotes the original HSIs data, and $\hat{y_n}$ denotes the true classification of d_n.

D. Communication Model

This section describes the system's communication link, which involves two key components. The local satellite communicates with neighboring satellites through the ISL in the Ka-band. Additionally, the satellite transmits the processed HSI data to the ground service center via the downlink, also in the Ka-band. In the ISL, the ground service center sends task assignment commands to the local satellite, directing it to transmit data to neighboring satellite m. The channel gain $h_{1,m}$ for this transmission is expressed as

$$h_{1,m} = 1/\left(4\pi d_{1,m} f/c\right)^2, \quad (9)$$

where f is the carrier frequency and c is the speed of light. $d_{1,m}$ is the distance between the local and neighboring satellites, denoted as

$$d_{1,m} = \sqrt{0 + (y_m - y_1)^2 + (z_m - z_1)^2}. \quad (10)$$

Thus the transmission data rate between ISL is obtained as [38]

$$r_{1,m} = B_{1,m} \log_2\left(1 + \frac{pg\,|h_{1,m}|^2}{\sigma^2}\right), \quad (11)$$

where $B_{1,m}$ is the channel bandwidth, p is the transmit power of the local satellite, g is the antenna gain of the local satellite, and σ^2 is the Gaussian noise of the corresponding link. Then the time consumed by local satellite to transmit data i to neighboring satellite m is

$$t^{tran}_{1,m(n)} = \frac{D_n}{\sum_{m \in \mathcal{M}} r_{1,m} \cdot \mathrm{I}\left[a_{n,m} = 1\right]}. \quad (12)$$

Similarly, the energy consumed is defined as

$$E^{tran}_{1,m(n)} = p^{tran}_1 \cdot t^{tran}_{1,m(n)}, \quad (13)$$

where p^{tran}_1 represents the energy consumed per second by the local satellite; in the downlink, the system employs two

methods to transmit data to the ground: (1) direct transmission of processed data from the satellite to the ground; and (2) transmission of satellite-processed data to the ground using IRS redirection. These two methods are used simultaneously to enhance transmission efficiency. In the case of direct data transmission, the channel gains $h_{m,g}$

$$h_{m,g} = \left(\frac{c}{4\pi f d_g}\right).\exp\left(\frac{-j2\pi f d_g}{c} + \frac{-K(f)d_g}{2}\right), \quad (14)$$

where j is the imaginary unit and $K(f)$ denotes the absorption coefficient of the transmission medium. In the case of data redirection transmission via IRS, IRS is deployed as a transmission mediator on the local satellite, which is located in the $Y-Z$ plane, and K_y and K_z denote the number of reflector units along the Y and Z axes, respectively. The whole number of reflector units is $K = K_y \times K_z$. We identify the first position in the lower left corner of the entire IRS reflector plate as the starting coordinate, denoted as $IR_1 = (0, IR_a, IR_b)$, and the k-th reflector element coordinate IR_k is

$$IR_k = (0, IR_a + (K_y - 1)\gamma_y, IR_b + (K_z - 1)\gamma_z), \quad (15)$$

where γ_y and γ_z denote the reflection unit spacing length. The transmission vector $\Delta r_{1,m}$ from the first reflection element IR_1 to the satellite m is denoted by

$$\Delta r_{1,m} = l_m - IR_1 = (0, y_m - IR_a, z_m - IR_b). \quad (16)$$

The difference Δr_k between the first reflection element and the k-th reflection element is defined as

$$\Delta r_k = IR_k - IR_1 = (0, (K_y - 1)\gamma_y, (K_z - 1)\gamma_z). \quad (17)$$

Therefore, the phase difference between the signals reflected by the first reflection unit and the k-th reflection unit original in the IRS θ_k^m is

$$\begin{aligned}\theta_k^m &= \frac{2\pi f}{c}\frac{\Delta r_n^T}{|\Delta r_k|}\Delta r_{1,m} \\ &= \frac{2\pi f}{|\Delta r_k|\, c}\left(\left(y_m - IR_a\right)\left(k_y - 1\right)\gamma_y\right. \\ &\quad \left. + \left(z_m - IR_b\right)\left(k_z - 1\right)\gamma_z\right). \end{aligned} \quad (18)$$

Meanwhile, the transmission vector $\Delta r_{1,g}$ from the first reflection unit of the IRS to the ground service center is: $\Delta r_{1,g} = IR_1 - l_g = (0, IR_a, IR_c)$. Similarly, the phase difference between the first reflector element transmission and the k-th reflector element transmission to the ground service center signal

$$\begin{aligned}\theta_k^g &= \frac{2\pi f}{c}\frac{\Delta r_k^T}{|\Delta r_k|}\Delta r_{1,g} \\ &= \frac{2\pi f}{|\Delta r_k|\, c}(IR_a(K_y - 1)\gamma_y - IR_b(K_z - 1)\gamma_z). \end{aligned} \quad (19)$$

Therefore, the cascaded channel gain $h'_{m,g}$ over the IRS connection is defined as

$$h'_{m,g} = \left(\frac{c}{8\sqrt{\pi^3} f d'_{m,g}}\right).\exp\left(\frac{-j2\pi f d'_{m,g}}{c} + \frac{-K(f)d'_{m,g}}{2}\right), \quad (20)$$

where $d'_{m,g} = \|\Delta r_g\|_2 + \|\Delta r_m\|_2$, where $\|\Delta r_g\|_2$ denotes the distance between the ground service center and the first reflector unit of the IRS, and $\|\Delta r_m\|_2$ denotes the distance between the first reflection unit of the IRS and the satellite m. Therefore, the channel gain $h''_{m,g}$ for transmitting data through IRS is defined as

$$h''_{m,g} = h'_{m,g} e_m \Psi_k e_g, \quad (21)$$

where $e_m = (\exp(j\theta_1^m), \exp(j\theta_2^m), \ldots, \exp(j\theta_n^m))$, $e_g = (\exp(j\theta_1^g, \exp(j\theta_2^g, \ldots, \exp(j\theta_k^g))^T$, $\Psi_k = diag(\exp(j\psi_1, \exp(j\psi_2, \ldots, \exp(j\psi_k,)$ denotes the phase shift diagonal matrix of reflection units, where ψ_k denotes the phase shift of the w-th reflection unit. Thus, the rate $R_{m,g}$ at which the satellite m transmits data to the ground service center is denoted as

$$R_{m,g} = B_m \log_2\left(1 + \frac{p_m g_m \left|h_{m,g} + h''_{m,g}\right|^2}{\sigma^2}\right), \quad (22)$$

where B_m denotes the channel bandwidth allocated to each satellite, p_m denotes the transmission power of satellite m, g_m denotes the antenna gain of satellite m. The time $t_{m(n),g}^{tran}$ consumed to process the data on satellite m and transmit the selected features back to the ground is denoted as

$$t_{m(n),g}^{tran} = \frac{b\sum_{l\in\mathcal{L}} x_{n,l}}{\sum_{m\in\mathcal{M}} R_{m,g}\cdot \mathrm{I}\left[a_{n,m}=1\right]}, \quad (23)$$

where b denotes the size of a single feature with a fixed shape. Meanwhile, the energy consumed by the downlink $E_{m(n),g}^{tran}$ is denoted as

$$E_{m(n),g}^{tran} = p_m \cdot t_{m(n),g}^{tran}. \quad (24)$$

E. Problem Formulation

In the whole system, the local satellite transmits the HSI to different neighboring satellites, the individual satellites process the data, and finally transmit the selected features to the ground, so the energy consumption E_n^{total} belonging to the HSI n is denoted as

$$E_n^{total} = E_{1,m(n)}^{tran} + E_{m(n)}^{comp} + E_{m(n),g}^{tran}. \quad (25)$$

During the satellite contact window, the system aims to minimize energy consumption while optimizing the classification performance by assigning the HSI data to different satellites for processing and transmitting the processed HSI data to the ground center. Therefore, the utility function U_n for processing HSI n is defined as

$$U_n = \omega_1 A_n - (1-\omega_1)\omega_2 E_n^{total}, \quad (26)$$

where $\omega_1 (0 \le \omega_1 \le 1)$ is a weight factor that balances the data classification performance with the energy consumption of the

system, and ω_2 is a factor used to map the energy consumption to the same level as the classification performance. Our optimization objective is to maximize the sum of utilities of all HSIs by selecting appropriate satellite allocation schemes and suitable subsets of bands, considering constraints such as energy and resources. Thus, the optimization problem can be formulated as

$$\begin{aligned}
&\max_{a,x,\psi} \sum_{m\in\mathcal{M}} \sum_{n\in\mathcal{N}} U_n \\
&\text{s.t.} \quad (\text{C1}): a_{n,m} \in \{0,1\}, \forall n, m, \\
&\qquad (\text{C2}): \sum_{m=1}^{M} a_{n,m} = 1, \\
&\qquad (\text{C3}): x_{n,l} \in \{0,1\}, \forall n, l, \\
&\qquad (\text{C4}): A_n \geq A^{target}, \forall n, \\
&\qquad (\text{C5}): 0 \leq \psi_k \leq 2\pi, \forall k, \\
&\qquad (\text{C6}): \sum_{m=1}^{M} a_{n,m} B_m \leq B, \forall n, \\
&\qquad (\text{C7}): \sum_{n=1}^{N} a_{n,m} S_{m(n)} \leq F_m, \forall m, \\
&\qquad (\text{C8}): \sum_{n=1}^{N} E_n^{total} \leq C + p_h \cdot T_{m(n)}^{max}, \forall m, \\
&\qquad (\text{C9}): t_{m(n)}^{comp} + t_{1,m(n)}^{tran} + t_n^{tran} \leq T_{m(n)}^{max}, \forall n, m. \quad (27)
\end{aligned}$$

The optimization problem seeks to determine the optimal task allocation $a_{n,m}$, HSI band selection $x_{n,l}$, and IRS phase shift ψ_w, aiming to minimize system energy consumption and maximize classification performance. The problem is subject to several constraints ensuring system feasibility and efficiency. Specifically, constraints (C1) and (C2) ensure that each HSI task is assigned to exactly one satellite, which can be either the local satellite or one of the neighboring satellites. Constraints (C3) and (C4) optimize feature subset selection $x_{n,l}$ to meet the target classification performance A^{target}. The IRS phase shift ψ_w, as specified in (C5), is constrained within $[0, 2\pi]$. Constraint (C6) ensures the total bandwidth for each task does not exceed the system's capacity B, while (C7) ensures satellites have sufficient resources F_m for their tasks. Considering the limited solar energy harvesting capability and energy constraints of LEO satellites, constraint (C8) strictly limits the total energy consumption to within the harvested energy during the contact window, which is fundamentally different from conventional ground-based systems that have relatively stable power supplies. Finally, constraint (C9) ensures that the total delay, including transmission and processing time, does not exceed the maximum allowable latency $T_{m(n)}^{max}$, which is particularly challenging given the short contact window of LEO satellites, where rapid and efficient data processing is crucial to maintaining reliable communications. This problem belongs to the NP-hard MINLP problem, which is difficult to be solved effectively by traditional optimization methods.

III. THE JFIO FRAMEWORK

A. JFIO Framework Overview

As shown in Fig. 2, the proposed joint feature iterative optimization (JFIO) framework consists of three alternating phases. First, to enhance the robustness of task offloading under dynamic network conditions, we introduce a long short-term memory (LSTM)-based link prediction module before the graph attention network (GAT). The LSTM model predicts future link quality based on historical SNR, azimuth and elevation angles, and recent bandwidth measurements, providing estimated data rates as additional features for the GAT input. The GAT model then analyzes satellite resource distribution and task conditions to generate an optimal task offloading scheme. Second, the offloading scheme is fused with HSI data in the feature fusion module to construct enriched feature representations fed into the multi-feature attention capsule network (MACN) for sub-band selection. Finally, the outputs of GAT and MACN are processed through a shared representation layer to guide IRS phase-shift optimization. By integrating a feedback mechanism and joint loss function, the system iteratively optimizes task allocation, spectral feature selection, and IRS configuration to enhance overall performance. A detailed description is provided in the following section.

B. Offloading Scheme Generation

In this subsection, we discuss the task offloading scheme. The input information to the GAT model consists of an adjacency matrix $\mathbf{A}_1 \in \mathbb{R}^{(M+I)\times(M+I)}$ and a vector of feature representations of the nodes $\mathbf{H} = \{\mathbf{h}_1, \mathbf{h}_2, \ldots, \mathbf{h}_{M+N}\}, \mathbf{h}_i \in R^F$, where M denotes the number of satellites, N denotes the number of HSIs, and the total number of nodes is $M + N$. The feature dimension of each node is F.

To enhance the accuracy and robustness of task offloading decisions under dynamic network conditions, we integrate a long short-term memory (LSTM) based link prediction module before the GAT model [4]. The LSTM model takes historical link quality data, specifically the signal-to-noise ratio (SNR), as input and predicts the future link quality $\hat{\mathbf{Q}}_i$. These predicted values are treated as additional features and combined with the existing satellite and task features to form comprehensive input representations for the GAT model. The input to the LSTM prediction network contains key parameters such as the azimuth angle, elevation angle at each time step, and recent bandwidth measurements, allowing the model to capture temporal dependencies and fluctuations in link quality. The output of the LSTM model is the predicted SNR, which is then transformed into the corresponding data rate $\mathbf{R}_i$ according to the communication model. By incorporating these predicted data rates as features, we improve the resilience of the task offloading strategy against varying environmental conditions and unpredictable link fluctuations.

For satellite nodes, $\mathbf{h}_i$ encodes crucial information such as computational resources, communication bandwidth, energy availability, and the predicted link quality obtained from the LSTM model. For HSI task nodes, $\mathbf{h}_i$ encapsulates details

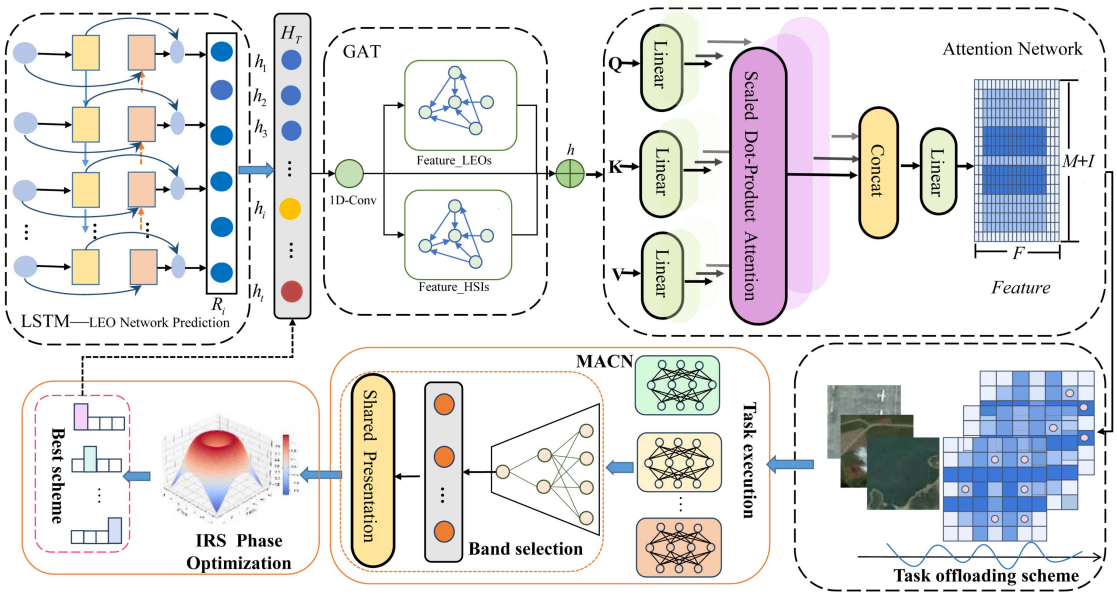

Fig. 2. The structure of the proposed JFIO Framework.

such as processing demand, data volume, and bandwidth requirements, ensuring a comprehensive representation of system constraints and requirements. This integration significantly improves the task offloading decision-making process, as it allows the model to proactively adapt to changing link conditions while maximizing the overall system utility.

First, the model captures the feature relationship between each node and its neighbors through local structure learning. For each node i, its features are mapped to a new feature space $\mathbf{W}\mathbf{h}_i$ by linear transformation, where $\mathbf{W} \in \mathbb{R}^{F' \times F}$ is the learnable weight matrix and F' is the transformed feature dimension. This transformation enables the model to learn higher-level representations, facilitating more effective task assignment. The nonlinear function is then used to compute the attention coefficients e_{ij} of node i and its neighbor node j. The attention coefficients of all neighboring nodes are normalized using the softmax function

$$\alpha_{ij} = \frac{\exp\left(e_{ij}\right)}{\sum_{l \in \tilde{\mathcal{N}(i)}} \exp\left(e_{il}\right)}, \tag{28}$$

where $\tilde{\mathcal{N}(i)}$ denotes the set of neighbor nodes of node i. Then all the neighboring nodes are subjected to feature aggregation

$$\mathbf{h}_i' = \sigma\left(\sum_{j \in \tilde{\mathcal{N}(i)}} \alpha_{ij} \mathbf{h}_j\right), \tag{29}$$

where σ is the $ReLU$ activation function. This aggregation mechanism effectively captures the dependencies among nodes, allowing each node to dynamically adjust its feature representation based on its local neighborhood. When all the nodes have undergone the above operation, the first-order neighborhood structure feature representation matrix is obtained $\mathbf{H}' = \{\mathbf{h}_1', \mathbf{h}_2', \ldots, \mathbf{h}_{\tilde{\mathcal{N}}}'\} \in \mathbb{R}^{(M+I) \times F'}$. This representation not only encodes localized interactions between task nodes and satellite nodes but also serves as a crucial input for subsequent global attention learning.

After local learning, the global structure is learned through the multi-head attention mechanism. A 2-layer graph attention network is employed to capture both local and high-level graph representations. Each GAT layer utilizes 4 attention heads, and the outputs are concatenated to retain comprehensive multi-head attention information. For each node i, its feature vector $\mathbf{h}_i$ is converted into query, key, and value representations. For the z-th attention head

$$\mathbf{Q}_i^{(z)} = \mathbf{W}_Q^{(z)} \mathbf{h}_i', \mathbf{K}_i^{(z)} = \mathbf{W}_K^{(z)} \mathbf{h}_i', \mathbf{V}_i^{(z)} = \mathbf{W}_V^{(z)} \mathbf{h}_i', \tag{30}$$

where $\mathbf{W}_Q^{(z)}, \mathbf{W}_K^{(z)}, \mathbf{W}_V^{(z)} \in \mathbb{R}^{F_h \times F'}$ are the learnable projection matrices for query, key, and value mappings. The attention coefficient $e_{ij}^{(z)}$ between nodes is computed as

$$e_{ij}^{(z)} = \frac{(\mathbf{Q}_i^{(z)})^{\mathrm{T}} \mathbf{K}_j^{(z)}}{\sqrt{F_h}}. \tag{31}$$

This global attention mechanism enables long-range dependencies to be captured, ensuring that task allocation decisions are informed by a holistic view of the network. The attention coefficients of all neighboring nodes are then normalized, and the features of neighboring nodes are aggregated using the weighted sum

$$\mathbf{h}_i^{(z)''} = \sum_{j \in \tilde{\mathcal{N}(i)}} \beta_{ij}^{(z)} \mathbf{V}_j^{(z)}, \tag{32}$$

where $\beta_{ij}^{(z)}$ is the normalized attention coefficient of node j with respect to node i, and $\mathbf{V}_j^{(z)}$ is the corresponding value vector. The outputs from all attention heads are then concatenated, forming a richer feature representation $\mathbf{h}_i''' = \mathrm{Concat}(\mathbf{h}_i^{(1)''}, \mathbf{h}_i^{(2)''}, \ldots, \mathbf{h}_i^{(H)''})$.

Finally, the concatenated features are mapped to the output space through a linear transformation: $\mathbf{H}^{\text{out}} = \mathbf{W}_{out}\mathbf{h}_i'''$, where $\mathbf{H}^{\text{out}}$ represents the final feature dimension output. Next, the global feature representation is inputted into an MLP, which consists of one input layer, five hidden layers, and one output layer. The output is the task assignment probability of each node, transformed into a probability distribution matrix via the $softmax$ activation function. The probability distribution matrix is then used to obtain the optimal allocation scheme matrix $\mathbf{A}$. Specifically, for each task n, the satellite m with the highest assignment probability is selected

$$a_{n,m} = \begin{cases} 1 & \text{if } m = \arg\max_m p_{i,m}, \\ 0 & \text{otherwise.} \end{cases} \tag{33}$$

This decision-making process ensures that each task is allocated to the most suitable satellite based on learned feature representations and global attention mechanisms. By traversing the allocation matrix, we obtain the final optimal allocation decision $a_{n,m}$.

C. Band Selection Optimization

In this subsection, we discuss the HSI band selection model. To perform satellite band selection of HSIs, the features of the task offloading scheme and the HSI features must first be mapped to the same feature space. The HSI data is represented as a three-dimensional tensor $\mathbf{X} \in \mathbb{R}^{H\times W\times B}$, where H and W are the spatial resolution, and B is the number of spectral bands. Each pixel contains spectral information from multiple bands.

The offloading scheme feature matrix $\mathbf{A}$ is transformed to the same feature space as the HSI data by a linear mapping: $\mathbf{A}' = \text{ReLU}(\mathbf{W}_e\mathbf{A}) \in \mathbb{R}^{H\times W\times d}$, where d is the mapped feature dimension and $\mathbf{W}_e \in \mathbb{R}^{M\times d}$ is the mapping matrix. The features $\mathbf{A}'$ and $\mathbf{X}$ are fused along the channel dimension via pixel-wise concatenation

$$\mathbf{X}'(i,j,:) = \mathbf{concat}(\mathbf{X}(i,j,:), \mathbf{A}'(i,j,:)). \tag{34}$$

The resulting tensor $\mathbf{X}' \in \mathbb{R}^{H\times W\times(B+d)}$ contains both HSI band and task offloading decision information, which is input to the MACN. The MACN consists of three key modules: a convolutional feature extraction module, a multi-feature attention module, and a capsule network. The convolutional module extracts low-level features to generate the feature map $\mathbf{F}_c \in \mathbb{R}^{H_c\times W_c\times d_c}$, where $H_c = 8$, $W_c = 9$, and $d_c = 256$.

In the multi-feature attention module, we adopt the convolutional block attention module (CBAM) [39] to enhance feature discrimination by jointly modeling spectral and spatial dependencies. CBAM sequentially applies channel and spatial attention to refine feature representations. Specifically, the channel attention module computes channel-wise attention weights $\mathbf{M}_{ch}$ by applying both average and max pooling operations to the input feature map $\mathbf{F}_c$, followed by a shared multi-layer perceptron (MLP). These weights emphasize informative spectral bands and are used to reweight $\mathbf{F}c$. Subsequently, the spatial attention module enhances the localization of salient spatial features by performing average and max pooling along the channel dimension of the reweighted features, followed by a 7×7 convolution to generate spatial attention weights $\mathbf{M}_{sp}$. The final refined feature map, denoted as $\mathbf{F}_{CBAM} \in \mathbb{R}^{8\times 9\times 256}$, captures both spectral and spatial importance and is fed into subsequent capsule layers for feature abstraction.

The feature map $\mathbf{F}_{CBAM}$ from the CBAM module is passed into the capsule network, which consists of three components: the main capsule layer, dynamic routing, and the classification capsule layer. First, the main capsule layer generates multi-dimensional capsule vectors for local regions in the feature map. This is done through a convolutional operation applied to the input feature map $\mathbf{F}_{CBAM}$, resulting in a capsule matrix $\mathbf{V}_p \in \mathbb{R}^{8\times 9\times d_p}$.

To improve feature representation accuracy and robustness, we utilize dynamic routing to adjust the connection weights between capsules [40]. The connection weights $c_{i,j,\check{k}}$ are computed using the softmax function

$$c_{i,j,\check{k}} = \frac{\exp(b_{i,j,\check{k}})}{\sum_{k'}\exp(b_{i,j,k'})}, \tag{35}$$

where $b_{i,j,\check{k}}$ is the initial coupling score between the capsules, which is refined during the routing process.

Finally, the classification capsule layer generates a d_c-dimensional capsule vector $\mathbf{v}_m$ for each sub-band class. The band selection is determined based on the length of the capsule vector $\mathbf{v}_m$. If the length exceeds a predefined threshold ε, the corresponding band is selected

$$x_{n,l} = \begin{cases} 1 & \text{if } ||\mathbf{v}_m|| > \varepsilon \\ 0 & \text{otherwise} \end{cases}, \tag{36}$$

where $x_{n,l}$ indicates whether the l-th spectral band is selected. The selected bands are then utilized to guide the subsequent IRS phase shift optimization.

D. IRS Phase Shift Optimization

After obtaining the optimal allocation scheme $a_{n,m}$ and selected features $x_{n,l}$, we proceed with IRS phase shift optimization using the Hippo Optimization (HO) algorithm [41]. We choose the HO algorithm for its efficient balance between exploration and exploitation. HO mimics defensive and developmental strategies, allowing it to escape local optima while maintaining computational efficiency. In the context of IRS phase shift optimization, where the problem is non-convex and high-dimensional, traditional gradient-based methods often suffer from slow convergence and suboptimal solutions. HO's adaptive mechanism makes it particularly suitable for this problem. The phase shift angles of the IRS cells are treated as individual solutions. Initial phase shifts are randomly generated and updated iteratively based on the exploration phase, where phase shifts are adjusted if performance fails to improve, mimicking a defensive strategy to avoid local optima

$$\psi_k^{(t+1)} = \psi_k^{(t)} + r\cdot(D_{\text{best}} - \psi_k^{(t)}), \tag{37}$$

where $\psi_k^{(t)}$ and $\psi_k^{(t+1)}$ are the current and updated phase shift angles, r is a random number, and D_{best} is the optimal IRS configuration.

Algorithm 1: Joint HSI Processing With JFIO in the Contact Window.

Input: Set of satellites $\mathcal{M}$, set of HSIs $\mathcal{N}$, IRS configuration $\mathcal{K}$, satellite and HSI features $\mathbf{H}$, historical link quality data $\mathbf{Q}$, maximum number of iterations T.
Output: Optimized task offloading strategy $\mathbf{A}$, selected hyperspectral bands $\mathbf{X}$, IRS phase shifts Ψ.

Initialize: $t \leftarrow 0$, $\mathbf{A}_0$, $\mathbf{X}_0$, Ψ_0.
Predict future link quality using LSTM.
  for each satellite $m_i \in \mathcal{M}$ **do**
    Extract historical link quality data $\mathbf{Q}_i$.
    Predict future link quality $\hat{\mathbf{Q}}_i \leftarrow \text{LSTM}(\mathbf{Q}_i)$.
    Transform predicted SNR to data rate R_i.
    Augment satellite feature embedding $\mathbf{h}_i \leftarrow [\mathbf{h}_i, R_i]$.
  end for
  while $t < T$ **do**
    for each satellite $m_i \in \mathcal{M}$ **do**
      Extract satellite feature embedding $\mathbf{h}_i \leftarrow \text{1D-Conv}(\mathbf{H}_i)$.
      for each HSI $n_j \in \mathcal{N}$ **do**
        Compute attention score e_{ij} between m_i and n_j.
      end for
      Aggregate task information for m_i.
    end for
    Update task offloading strategy $\mathbf{A}^{(t)}$ with GAT.
    Perform band selection $\mathbf{X}^{(t)} \leftarrow \text{MACN}(\mathbf{X}, \mathbf{A}^{(t)})$.
    Optimize IRS phase shifts $\Psi^{(t)}$ based on $\mathbf{A}^{(t)}$ and $\mathbf{X}^{(t)}$.
    Compute loss $\mathcal{L}$ and update:

$$\mathbf{A}^{(t)}, \mathbf{X}^{(t)}, \Psi^{(t)} \leftarrow \text{Update}(\mathcal{L}).$$

    Update variables: $\mathbf{A}_0 \leftarrow \mathbf{A}^{(t)}$, $\mathbf{X}_0 \leftarrow \mathbf{X}^{(t)}$, $\Psi_0 \leftarrow \Psi^{(t)}$.
    if convergence criterion met **then**
      Break.
    end if
    Increment iteration: $t \leftarrow t + 1$.
  end while

If the defensive strategy does not improve performance, the system enters the development phase, where local search is applied to fine-tune phase shifts and achieve better coordination with the optimal allocation scheme $a_{n,m}$ and selected band $x_{n,l}$.

To ensure that the predicted allocation schemes are progressively close to the optimal scheme, we introduce a scheme update strategy where GAT is trained under unsupervised conditions, i.e., it does not rely on pre-labeled data samples. The optimization objective and constraints determine the loss function. We wish to satisfy all constraints simultaneously by minimizing the system's total energy consumption. Therefore, we design a hierarchical loss function [42], the loss function contains two parts: the optimization objective loss and the constraints loss

$$\mathcal{L}'(\theta) = \hat{a}_{n,m} E_n^{total} + \textstyle\sum_{z=1}^{4} g_z(f_\theta(\mathbf{A}(n), \mathbf{H}(n))). \quad (38)$$

For constraints $(\text{C6}) - (\text{C9})$, g_z is a penalty constraint, $g_z = \sum_{m=1}^{M} \max(0, \sum_{n=1}^{N} \hat{a}_{n,m} b_m - B)$ where $z = 1$. For the remaining constraints $(\text{C7}) - (\text{C9})$, similar penalty functions are applied, ensuring all constraints are simultaneously enforced. The parameter θ is optimized using the Adam optimizer to refine the predicted allocation scheme iteratively, ensuring its convergence to the optimal solution.

To improve classification performance, we design an objective function based on cross-entropy loss to measure the error between the predicted results and the actual labels. Specifically, let y_n denote the predicted classification confidence score for HSI task n, which represents the probability that the selected band features lead to a correct classification. This value is obtained from the MACN and can be expressed as $y_n = \sigma(f(\boldsymbol{x_n}; \theta_{MACN}))$, where $f(\cdot; \theta_{MACN})$ denotes the function implemented by θ_{MACN}, $\sigma(\cdot)$ is the softmax activation function, ensuring that the output is a probability value between 0 and 1. Meanwhile, to satisfy the (C4) constraint, we introduce a penalty function and control the selection of bands by regularization to prevent selecting too many or too few bands. Its expression is

$$\mathcal{L}''(\theta) = -\sum_{n=1}^{N} d_n \log y_n + \sum_{l=1}^{L} x_{n,l} \max(0, A^{target} - A_n). \quad (39)$$

Then, the combined loss function of the whole is constructed as

$$\mathcal{L}(\theta) = \delta_1 \mathcal{L}'(\theta) + (1 - \delta_1)\mathcal{L}''(\theta), \quad (40)$$

where δ_1 is the weight parameter used to balance task assignment and band selection optimization objectives. The problem is solved by minimizing $\mathcal{L}$, optimizing the offloading scheme and the band selection scheme step by step, and finally combining the IRS phase shift obtained by the HO algorithm. The pseudo-code of JFIO is given in Algorithm 1.

E. Computation Complexity Analysis

The computational complexity of JFIO differs between the training and inference phases, as the former requires iterative optimization and backpropagation, while the latter involves only forward computations. During training, the computational complexity is significantly higher due to the iterative updates of model parameters. The task offloading step using GAT involves computing attention scores and aggregating information across satellites and tasks, with a complexity of $O(L_G(MNF + MF^2))$ per forward pass, where L_G is the number of GAT layers, M is the number of satellites, N is the number of HSI tasks, and F is the feature dimension. Since backpropagation doubles the computations, this step alone incurs a complexity of $O(2L_G(MNF + MF^2))$ per iteration. Similarly, MACN performs feature extraction and selection with a complexity of $O(2L_C C d^2)$, where L_C is the number of routing iterations, C is the number of capsules, and d is the feature dimension. Additionally, IRS phase shift optimization involves iterative updates, contributing a complexity of $O(KI_{IRS})$, where K is the number of IRS elements and I_{IRS} is the number of iterations required for convergence. Given that JFIO undergoes multiple

TABLE II
DETAILS OF THE HSI DATASETS

Dataset	Size	Number of Classes
Indian Pines [45]	$145 \times 145 \times 200$	16
Botswana [45]	$1476 \times 256 \times 145$	14
HyRANK Dioni [46]	$250 \times 1376 \times 176$	14
HyRANK Loukia [46]	$249 \times 945 \times 176$	14

optimization steps over T iterations, the total training complexity is $O(T(2L_G(MNF + MF^2) + 2L_C C d^2 + KI_{IRS}))$, making training computationally expensive [4]. In contrast, the inference phase does not require backpropagation or iterative parameter updates, reducing the overall computational burden. Task offloading through GAT requires only a single forward pass, leading to a complexity of $O(L_G(MNF + MF^2))$, while MACN performs feature selection with a complexity of $O(L_C C d^2)$. The IRS phase shift optimization step, which is precomputed or determined through a lightweight closed-form solution, contributes a minimal complexity of $O(K)$. Consequently, the total inference complexity is $O(L_G(MNF + MF^2) + L_C C d^2 + K)$, which is significantly lower than the training complexity since no gradient computations or iterative updates are involved.

IV. EXPERIMENTAL SETTINGS

A. Evaluation Setup

Our simulation uses network data from the JPSS with Ka-band satellite links [43], [44], incorporating parameters like elevation angle, signal strength, and signal-to-noise ratio. We account for path loss and atmospheric attenuation, adjusting the ideal communication model to achieve a dynamic data rate fluctuating between 1 and 10 Mbps. For realistic satellite edge computing simulation, we selected four real HSI datasets. The detailed information of the datasets is summarized in Table II. To address the inconsistency in spatial and spectral dimensions across different datasets, we applied a unified preprocessing strategy. Specifically, all datasets were resized or padded with zero-filled sub-bands to a consistent shape of $150 \times 150 \times 200$, ensuring compatibility during joint training and evaluation.

B. The Execution of JFIO

We implemented the JFIO framework using PyTorch 1.9, with 70% of the dataset allocated for training and 30% for testing. The experimental environment consisted of an RTX 4070 Ti GPU, an Intel i7-13700 CPU (3.4GHz), and 64GB of RAM. The trained JFIO is deployed on Jetson TX2. With a power consumption of only 7.5W, it is suitable for deep learning tasks at the edge of low-orbit satellites with limited energy [4]. To ensure the effective integration of the task offloading and band selection modules, we unified their training hyperparameters: a learning rate of 0.001, a batch size of 32, and 50 iterations. The task offloading module utilizes a GAT with four attention heads and a Dropout rate of 0.5 to mitigate overfitting. Meanwhile, the band selection module employs a MACN with ten capsule units and a custom hybrid loss function, where the parameter $\delta_1 = 0.5$ balances the task classification loss and energy efficiency optimization. Both modules are optimized using the Adam optimizer to ensure stable convergence. In addition, weight factors $\omega_1, \omega_2 = 0.5$ are used to balance the contributions of the task offloading and band selection modules during optimization.

Additionally, a memory buffer was incorporated into the joint optimization module to store the system performance metrics from previous iterations, which aids in hyperparameter tuning and loss function refinement. To address the no-timeout constraint for HSIs, a penalty of 100 is applied to the total energy cost for any HSI that exceeds its allocated processing time. The IRS phase shift is optimized using the HO method, with a population size of 10 and 50 evolution rounds. Candidate solutions are generated through random phase shift angles, which are iteratively adjusted based on the optimal solution to enhance system performance.

In order to validate the effectiveness of the JFIO framework, we compared it with multiple benchmarking schemes.

1) *Random:* HSI data is randomly allocated to satellites, ten random offloading decisions are generated, and the decision with the highest utility is selected as the baseline performance.
2) *Greedy:* HSI data allocation is optimized using a greedy algorithm that selects the HSI with the longest processing time and assigns it to the satellite with the fastest processing speed to improve local efficiency.
3) *OEC-TA [13]:* Optimize HSI task allocation based on greedy strategy step by step, dynamically adjust edge computing resources to improve performance and utilization.
4) *FullBand:* Transmit all HSI data to ground for processing without band selection as an inefficient processing strategy. This serves as a reference for evaluating the benefits of onboard band selection.
5) *EGSSR [32]:* EGSSR combines graph convolutional networks to perform robust band selection using non-euclidean structural information and identify informative subsets of bands through ranking and clustering strategies.
6) *MaHSI [4]:* Based on multi-agent reinforcement learning, MaHSI models band selection as a utility maximization task to improve analytical accuracy and inference efficiency in dynamic environments.

V. EXPERIMENTAL RESULT

A. Overall Utility Comparison

In this experiment, we evaluated the effect of different numbers of LEOs on the HSI utility of the JFIO model processing by calculating the combined utility over the entire contact window.

Fig. 3 illustrates the average normalized sum of HSI utility for different methods. The results show that JFIO outperforms the other models with significant utility gains, particularly as the number of LEOs increases. For instance, JFIO achieves a 104% utility increase when the number of LEOs rises from 3 to 15. In contrast, the utility gains for the other models are smaller, with MaHSI increasing by 102% and EGSSR by only 90%. Specifically, at 6 LEOs, JFIO's utility is 20% higher than that of MaHSI, and at 9 LEOs, JFIO significantly outperforms the average of the

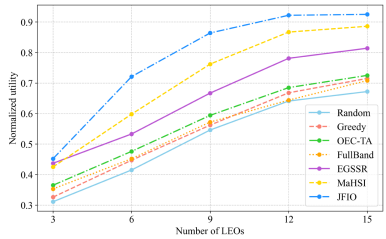

Fig. 3. HSI utility comparison of different approaches under different number of LEOs.

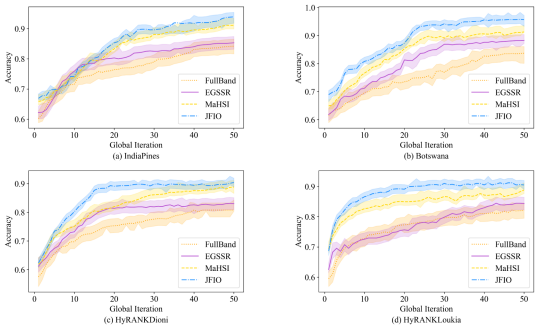

Fig. 4. Accuracy comparison of different methods.

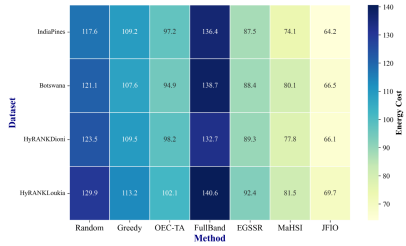

Fig. 5. Energy cost comparison of different methods.

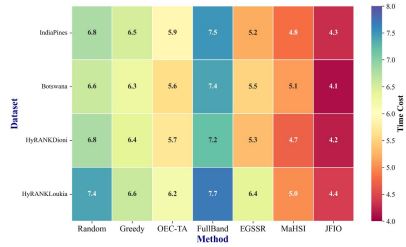

Fig. 6. Time cost comparison of different methods.

other methods. Notably, at 15 LEOs, JFIO leads MaHSI by 4% and surpasses EGSSR by 12%. This superior performance can be attributed to JFIO's integrated design that jointly considers task offloading, band selection, and IRS phase optimization. As the number of LEOs increases, the available computational and communication resources grow, which JFIO can effectively leverage due to its adaptive allocation mechanism. In contrast, MaHSI and EGSSR optimize only a single module and thus struggle to coordinate resource allocation holistically.

B. Classification Performance

With the number of LEOs fixed at 15, we compare the classification performance of JFIO against other band selection methods. Overall, JFIO achieves an average improvement in classification accuracy of 3%–6% across all datasets. Fig. 4 illustrates the average test accuracy across five experiments, with the solid curve representing the performance of each method. JFIO consistently outperforms the sub-optimal methods, exhibiting an accuracy improvement of 3.2%–3.6%. Moreover, the accuracy curve for JFIO shows a smaller shaded region, indicating lower variance and higher consistency across multiple experiments, which suggests a more stable learning process. The classification advantage comes from JFIO's attention-guided capsule network, which better preserves spatial-spectral features after band selection. Additionally, its joint optimization strategy ensures that selected bands are not only energy-efficient but also highly informative for classification.

C. Network Cost

We evaluate the average energy and time costs associated with HSI processing across different datasets. Fig. 5 illustrates that JFIO consistently outperforms all other methods in terms of energy efficiency, reducing energy consumption by 15% to 53% compared to traditional fixed bandwidth selection approaches. In scenarios with poor network conditions, JFIO demonstrates its capacity to effectively mitigate high energy consumption through intelligent bandwidth allocation and task optimization, achieving nearly a 50% reduction in energy expenditure compared to the FullBand strategy. This energy advantage is largely due to JFIO's dynamic task allocation mechanism, which avoids overloading any single node and reduces redundant transmissions. Furthermore, JFIO reduces energy overhead by 15% to 35% compared to adaptive methods such as Greedy and OEC-TA, showcasing its superior ability to dynamically adjust resource utilization in response to varying network conditions.

As shown in Fig. 6 in terms of time consumption, JFIO also exhibits significant improvements, achieving a reduction of 20% to 45% in time cost, particularly when compared to the FullBand strategy, with reductions of approximately 40% across different datasets. Even when compared to other advanced bandwidth selection methods, JFIO manages to reduce time consumption by 15% to 30%, underscoring its effectiveness in optimizing time overhead in both high-load and stable network environments. This time efficiency is critical in real-time HSI processing applications, where rapid decision-making and data transmission are essential.

D. Inference Time Measurement

To evaluate the inference efficiency of the proposed JFIO framework, we conducted 10 experimental runs on the Jetson TX2 and recorded the average inference time for various HSIs [4]. As shown in Fig. 7, JFIO consistently outperforms OEC-TA, EGSSR, and MaHSI, achieving a reduction of approximately 17% to 22% compared to OEC-TA, 10% to 15% compared to EGSSR, and 8% to 13% compared to MaHSI. The error bars in the figure indicate the standard deviation obtained

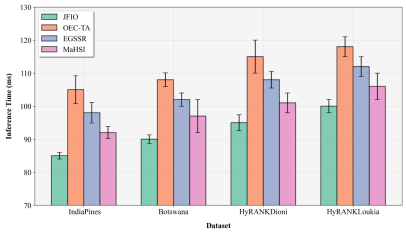

Fig. 7. Inference time comparison of different models on various datasets.

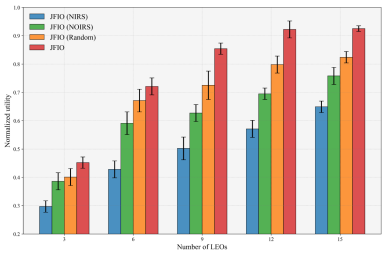

Fig. 8. Utility performance of JFIO under various IRS conditions.

from 10 independent runs, reflecting JFIO's stability and robustness even under fluctuating network conditions. Moreover, JFIO's model size is only 21.3 MB, making it lightweight and, therefore, particularly suitable for deployment on satellite edge devices with limited computational resources.

E. IRS Analysis

We evaluated JFIO's performance under various IRS conditions by calculating the combined utility for processing all HSI data within the contact window. Fig. 8 shows the results for different configurations: JFIO(NIRS), representing direct HSI transmission without IRS; JFIO(NOIRS), lacking phase shift optimization; and JFIO(RandomIRS), using randomly set IRS phase shifts. The results demonstrate that JFIO significantly outperforms JFIO(NIRS), achieving a 50%–58% improvement in utility, especially in low-density networks with fewer LEOs, where IRS optimization has a substantial impact. Even as the number of LEOs increases, JFIO maintains a 30%–39% utility advantage over JFIO(NIRS). Compared to JFIO(NOIRS), JFIO consistently shows a 20%–31% utility gain across all LEO configurations. While JFIO(RandomIRS) exhibits some fluctuation in utility depending on the LEO count, it slightly outperforms JFIO(NIRS) but remains well below the optimized JFIO. With 15 LEOs, phase shift optimization still results in a 20% utility increase. The utility gains stem from the IRS's ability to enhance transmission directionality and signal strength. JFIO's adaptive IRS controller optimizes reflection coefficients based on the joint feature representation, thereby improving throughput and reducing interference. Additionally, the error bars in Fig. 7 reflect the variability across multiple trials, highlighting the stability and consistency of JFIO's performance, particularly when IRS phase shift optimization is employed. These results demonstrate that JFIO improves utility and enhances transmission stability, making it highly effective across varying network densities and resource conditions.

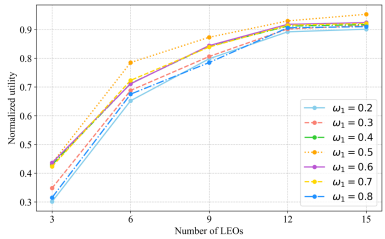

Fig. 9. Impact of different weight parameters w_1 on HSI utility.

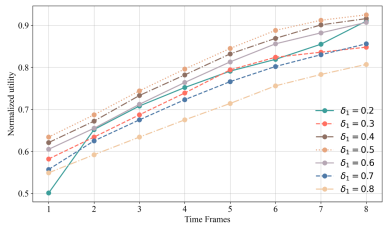

Fig. 10. Impact of different loss function weight parameters δ_1 on HSI utility.

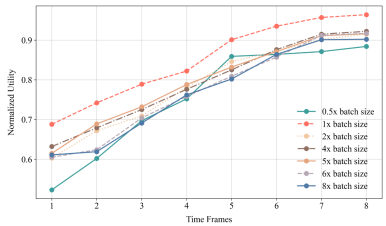

Fig. 11. Impact of memory buffer size on HSI utility.

F. Sensitivity Analysis

Fig. 9 illustrates the variation in utility value as a function of the weight parameter. Specifically, when the number of LEOs is limited, some HSIs are not processed within the available contact window, leading to increased energy consumption and, consequently, a reduced utility value. This effect is particularly pronounced at lower values of w_1, where the system's performance is more sensitive to the imbalance in resource allocation. As the number of LEOs increases, however, the utility value stabilizes, indicating improved system efficiency and stability. This leveling off of the utility curve suggests that the system becomes better adapted to the task processing demands, with increased LEOs ensuring more effective resource utilization and task completion within the optimal timeframe.

Fig. 10 illustrates the effect of varying loss function weighting coefficients on the model's training performance, with the vertical axis representing the average utility of HSI processing. At lower coefficients, such as $\delta_1 = 0.3$ or $\delta_1 = 0.4$, the model converges quickly, achieving higher utility early on. Medium-weight coefficients, such as $\delta_1 = 0.5$, yield the highest final utility, striking a balance between task classification and energy efficiency optimization. Higher coefficients, such as $\delta_1 = 0.7$ or $\delta_1 = 0.8$, result in slower initial convergence but are better suited for energy-efficiency tasks, supporting long-term sustainability. Overall, medium-weight coefficients offer the best trade-off, optimizing both classification accuracy and energy efficiency.

Fig. 11 illustrates the impact of varying memory buffer sizes on model training, with the vertical axis representing the average utility of HSI processing. The model achieves optimal performance at a memory buffer size of "1x" (i.e., the memory size equals the batch size), where utility is consistently the highest. This configuration efficiently utilizes memory resources, avoiding computational inefficiencies and resource wastage. As memory size increases from 0.5x to 1x, utility improves significantly. However, beyond 2x, the rate of utility gain diminishes, indicating that the model reaches an optimal memory configuration at 1x. Further increases in memory size yield minimal performance improvements and may introduce overheads due to inefficient resource allocation and data cache expansion.

VI. Conclusion

In this paper, we propose a novel IRS-assisted SEC system optimized for HSI processing, addressing the challenges of limited communication bandwidth, constrained onboard resources, and dynamic inter-satellite conditions. Our system leverages the cooperative capabilities of a local LEO satellite and multiple neighboring satellites, each equipped with edge computing units, to form a distributed computing network. The HSI processing task is formulated as a utility maximization problem that jointly considers task offloading, band selection, and communication efficiency. To effectively address this complex problem, we introduce the JFIO framework to process HSI tasks efficiently. The JFIO framework integrates a GAT for dynamic task offloading, a MACN for HSI band selection, and IRS phase shift optimization. Extensive experiments demonstrate that JFIO significantly outperforms traditional state-of-the-art methods in terms of task processing efficiency, adaptability, and energy consumption. The modular and extensible nature of JFIO provides a valuable reference for future research in multi-satellite cooperative computing, adaptive HSI processing, and intelligent satellite network design.

References

[1] Y. Zhang, P. Zhang, C. Jiang, S. Wang, H. Zhang, and C. Rong, "QoS aware virtual network embedding in space-air-ground-ocean integrated network," *IEEE Trans. Serv. Comput.*, vol. 17, no. 4, pp. 1712–1723, Jul./Aug. 2024.

[2] Q. Kong, X. Qu, S. Zhang, F. Yin, R. Lu, and B. Chen, "A secure satellite-edge computing framework for collaborative line outage identification in smart grid," *IEEE Trans. Serv. Comput.*, vol. 17, no. 3, pp. 761–775, May/Jun. 2024.

[3] P. Peng et al., "A survey on computation offloading in edge systems: From the perspective of deep reinforcement learning approaches," *Comput. Sci. Rev.*, vol. 53, 2024, Art. no. 100656.

[4] B. Zhu, S. Lin, Y. Zhu, and X. Wang, "Collaborative hyperspectral image processing using satellite edge computing," *IEEE Trans. Mobile Comput.*, vol. 23, no. 3, pp. 2241–2253, Mar. 2024.

[5] T. Pfandzelter, J. Hasenburg, and D. Bermbach, "Towards a computing platform for the LEO edge," in *Proc. 4th Int. Workshop Edge Syst., Analytics Netw.*, 2021, pp. 43–48.

[6] M. Zhao, C. Chen, L. Liu, D. Lan, and S. Wan, "Orbital collaborative learning in 6 G space-air-ground integrated networks," *Neurocomputing*, vol. 497, pp. 94–109, 2022.

[7] J. Feng, L. Liu, X. Hou, Q. Pei, and C. Wu, "QoE fairness resource allocation in digital twin-enabled wireless virtual reality systems," *IEEE J. Sel. Areas Commun.*, vol. 41, no. 11, pp. 3355–3368, Nov. 2023.

[8] H. Zhang, H. Zhao, R. Liu, X. Gao, and S. Xu, "Leader federated learning optimization using deep reinforcement learning for distributed satellite edge intelligence," *IEEE Trans. Serv. Comput.*, vol. 17, no. 5, pp. 2544–2557, Sep./Oct. 2024.

[9] O. Kodheli et al., "Satellite communications in the new space era: A survey and future challenges," *IEEE Commun. Surveys Tuts.*, vol. 23, no. 1, pp. 70–109, Firstquarter 2021.

[10] J. Du et al., "Profit maximization for multi-time-scale hierarchical DRL-Based joint optimization in MEC-Enabled air-ground integrated networks," *IEEE Trans. Commun.*, vol. 73, no. 3, pp. 1591–1606, Mar. 2025.

[11] Z. Xiao et al., "LEO satellite access network (LEO-SAN) toward 6 G: Challenges and approaches," *IEEE Wireless Commun.*, vol. 31, no. 2, pp. 89–96, Apr. 2024.

[12] C. Ding, Y. Li, Z. Lu, S. Wang, and S. Guo, "A resource-efficient feature extraction framework for image processing in IoT devices," *IEEE Trans. Mobile Comput.*, vol. 23, no. 1, pp. 42–55, Jan. 2024.

[13] Y. Zhang, C. Chen, L. Liu, D. Lan, H. Jiang, and S. Wan, "Aerial edge computing on orbit: A task offloading and allocation scheme," *IEEE Trans. Netw. Sci. Eng.*, vol. 10, no. 1, pp. 275–285, Jan./Feb. 2023.

[14] K. Wang, X. Wang, N. Zhao, X. Yang, H. Fang, and D. Niyato, "Uplink RSMA in LEO satellite communications: A perspective from generative artificial intelligence," *IEEE Trans. Veh. Technol.*, early access, Jun. 17, 2025, doi: 10.1109/TVT.2025.3579713.

[15] L. Liu, J. Feng, C. Wu, C. Chen, and Q. Pei, "Reputation management for consensus mechanism in vehicular edge metaverse," *IEEE J. Sel. Areas Commun.*, vol. 42, no. 4, pp. 919–932, Apr. 2024.

[16] H. Wu et al., "Container scheduling strategy based on image layer reuse and sequential arrangement in mobile edge computing," *IEEE Trans. Mobile Comput.*, vol. 24, no. 9, pp. 8700–8713, Sep. 2025.

[17] J. Du, M. Xu, S. S. Gill, and H. Wu, "Computation energy efficiency maximization for intelligent reflective surface-aided wireless powered mobile edge computing," *IEEE Trans. Sustain. Comput.*, vol. 9, no. 3, pp. 371–385, May/Jun. 2024.

[18] Z. Xu, G. Xu, H. Wang, W. Liang, Q. Xia, and S. Wang, "Enabling streaming analytics in satellite edge computing via timely evaluation of Big Data queries," *IEEE Trans. Parallel Distrib. Syst.*, vol. 35, no. 1, pp. 105–122, Jan. 2024.

[19] Y. Lee and J. P. Choi, "Connectivity analysis of mega-constellation satellite networks with optical intersatellite links," *IEEE Trans. Aerosp. Electron. Syst.*, vol. 57, no. 6, pp. 4213–4226, Dec. 2021.

[20] J. Yang, B. Du, D. Wang, and L. Zhang, "ITER: Image-to-pixel representation for weakly supervised HSI classification," *IEEE Trans. Image Process.*, vol. 33, pp. 257–272, 2024.

[21] A. U. G. Sankararao, P. Rajalakshmi, and S. Choudhary, "UC-HSI: UAV-Based crop hyperspectral imaging datasets and machine learning benchmark results," *IEEE Geosci. Remote Sens. Lett.*, vol. 21, 2024, Art. no. 5508005.

[22] C. Wang, Y. Zhang, Q. Li, A. Zhou, and S. Wang, "Satellite computing: A case study of cloud-native satellites," in *Proc. 2023 IEEE Int. Conf. Edge Comput. Commun.*, Chicago, IL, USA, 2023, pp. 262–270.

[23] Z. Song, Y. Hao, Y. Liu, and X. Sun, "Energy-efficient multiaccess edge computing for terrestrial-satellite Internet of Things," *IEEE Internet Things J.*, vol. 8, no. 18, pp. 14202–14218, Sep. 2021.

[24] C. Mei, C. Gao, Y. Xing, X. Bian, and B. Hu, "An energy consumption minimization optimization scheme for HAP-Satellites edge computing," in *Proc. IEEE 22nd Int. Conf. Commun. Technol.*, Nanjing, China, 2022, pp. 857–862.

[25] S. Sthapit, S. Lakshminarayana, L. He, G. Epiphaniou, and C. Maple, "Reinforcement learning for security-aware computation offloading in satellite networks," *IEEE Internet Things J.*, vol. 9, no. 14, pp. 12351–12363, Jul. 2022.

[26] Q. Li et al., "Battery-aware energy optimization for satellite edge computing," *IEEE Trans. Serv. Comput.*, vol. 17, no. 2, pp. 437–451, Mar./Apr. 2024.

[27] I. Leyva-Mayorga et al., "Satellite edge computing for real-time and very-high resolution earth observation," *IEEE Trans. Commun.*, vol. 71, no. 10, pp. 6180–6194, Oct. 2023.

[28] X. Zhang et al., "Energy-efficient computation peer offloading in satellite edge computing networks," *IEEE Trans. Mobile Comput.*, vol. 23, no. 4, pp. 3077–3091, Apr. 2024.

[29] H. Wu, X. Yang, and Z. Bu, "Task offloading with service migration for satellite edge computing: A deep reinforcement learning approach," *IEEE Access*, vol. 12, pp. 25844–25856, 2024.

[30] G. Cui, P. Duan, L. Xu, and W. Wang, "Latency optimization for hybrid GEO–LEO satellite-assisted IoT networks," *IEEE Internet Things J.*, vol. 10, no. 7, pp. 6286–6297, Apr. 2023.

[31] Q. Tang et al., "Joint service deployment and task scheduling for satellite edge computing: A two-timescale hierarchical approach," *IEEE J. Sel. Areas Commun.*, vol. 42, no. 5, pp. 1063–1079, May 2024.
[32] Y. Cai, Z. Zhang, X. Liu, and Z. Cai, "Efficient graph convolutional self-representation for band selection of hyperspectral image," *IEEE J. Sel. Topics Appl. Earth Observ. Remote Sens.*, vol. 13, pp. 4869–4880, 2020.
[33] S. Li, W. Song, L. Fang, Y. Chen, P. Ghamisi, and J. A. Benediktsson, "Deep learning for hyperspectral image classification: An overview," *IEEE Trans. Geosci. Remote Sens.*, vol. 57, no. 9, pp. 6690–6709, Sep. 2019.
[34] J. Wu et al., "Two-Stage Deep Energy Optimization in IRS-Assisted UAV-Based Edge Computing Systems," *IEEE Trans. Mob. Comput.*, vol. 24, no. 1, pp. 449–465, Jan. 2025.
[35] S. Mao et al., "Joint beamforming and reflecting design for IRS-Aided wireless powered over-the-air computation and communication networks," *IEEE Trans. Commun.*, vol. 72, no. 4, pp. 2216–2231, Apr. 2024.
[36] B. Zheng, S. Lin, and R. Zhang, "Intelligent reflecting surface-aided LEO satellite communication: Cooperative passive beamforming and distributed channel estimation," *IEEE J. Sel. Areas Commun.*, vol. 40, no. 10, pp. 3057–3070, Oct. 2022.
[37] X. Liu, M. Lin, M. Tan, H. Guo, J. Ouyang, and T. Q. S. Quek, "Location-based downlink transmission scheme for IRS-Aided integrated satellite-terrestrial networks," *IEEE Trans. Commun.*, vol. 72, no. 2, pp. 1090–1104, Feb. 2024.
[38] P. Shaik, K. K. Garg, P. K. Singya, V. Bhatia, O. Krejcar, and M. -S. Alouini, "On performance of integrated satellite HAPS ground communication: Aerial IRS node vs terrestrial IRS node," *IEEE Open J. Commun. Soc.*, vol. 5, pp. 3775–3791, 2024.
[39] L. Xu, S. Cao, X. Fu, X. Qin, X. Li, and T. A. Gulliver, "Mobile power allocation intelligent optimization algorithm for cooperative NOMA network based on CBAM-BiLSTM," *IEEE Trans. Veh. Technol.*, vol. 73, no. 5, pp. 7131–7139, May 2024.
[40] Q. Xu, K. Chen, X. Sun, Y. Zhang, H. Li, and G. Xu, "Pseudo-siamese capsule network for aerial remote sensing images change detection," *IEEE Geosci. Remote Sens. Lett.*, vol. 19, 2022, Art. no. 6000405.
[41] M. H. Amiri, N. M. Hashjin, M. Montazeri, S. Mirjalili, and N. Khodadadi, "Hippopotamus optimization algorithm: A novel nature-inspired optimization algorithm," *Sci. Rep.*, vol. 14, 2024, Art. no. 5032.
[42] J. Achiam, D. Held, A. Tamar, and P. Abbeel, "Constrained policy optimization," in *Proc. 34th Int. Conf. Mach. Learn.*, 2017, pp. 22–31.
[43] D. Vasisht, J. Shenoy, and R. Chandra, "L2D2: Low latency distributed downlink for LEO satellites," in *Proc. ACM SIGCOMM 2021 Conf.*, 2021, pp. 151–164.
[44] "L2D2 satellite datasets," 2021. [Online]. Available: https://github.com/ConnectedSystemsLab/L2D2
[45] Grupo de Inteligencia Computacional, "Hyperspectral remote sensing scenes," 2021. [Online]. Available: https://www.ehu.eus/ccwintco/index.php/Hyperspectral_Remote_Sensing_Scenes
[46] K. Karantzalos, C. Karakizi, Z. Kandylakis, and G. Antoniou, "HyRANK hyperspectral satellite dataset i (version v001)," *Zenodo*, Apr. 2018, doi: 10.5281/zenodo.1222202.

Xiaoteng Yang is currently working toward the PhD degree in communication and information systems with Xidian University, Xi'an, China. His current research interests include edge computing, resource assignment, satellite networks and stochastic network optimization.

Jie Feng (Member, IEEE) received the PhD degree in communication and information systems from Xidian University, China, in 2020. From 2018 to 2019, she was with Carleton University, Ottawa, ON, Canada, as a visiting Ph.D. student. She is currently an associate professor with the Department of Electrical Engineering and Computer Science, Xidian University, Xian, China. Her current research interests include mobile-edge computing, blockchain, deep reinforcement learning, the device to device communication, resource assignment, convex optimization, and stochastic network optimization.

Lei Liu (Member, IEEE) received the BEng degree in communication engineering from Zhengzhou University, Zhengzhou, China, in 2010, and the MSc and PhD degrees in communication engineering from Xidian University, Xi'an, China, in 2013 and 2019, respectively. From 2013 to 2015, he was with a technology company. From 2018 to 2019, he was a visiting Ph.D. student with the University of Oslo, Oslo, Norway. He is currently a lecturer with the Department of Electrical Engineering and Computer Science, Xidian University. His research interests include vehicular ad hoc networks, intelligent transportation, mobile edge computing, and the Internet of Things.

Qingqi Pei (Senior Member, IEEE) received the BS, MS, and PhD degrees in computer science and cryptography from Xidian University, Xi'an, China, in 1998, 2005, and 2008, respectively. He is currently a professor and member with the State Key Laboratory of Integrated Services Networks, Xidian University, where he is also the director of the Shaanxi Key Laboratory of Blockchain and Secure Computing. His research interests include digital contents protection and wireless networks and security. Dr. Pei is a professional member of the Association for Computing Machinery. He is a senior member of the Chinese Institute of Electronics and the China Computer Federation.

Shahid Mumtaz (Senior Member, IEEE)) is currently an IET Fellow, IEEE ComSoc Lecturer, and an ACM Distinguished Speaker. He has authored four technical books, 12 book chapters, and more than 300 technical articles (more than 200 IEEE Journals/Transactions, more than 100 conferences, and two IEEE best paper awards) in mobile communications. Dr. Mumtaz was the recipient of the NSFC Researcher Fund for Young Scientist in 2017 from China and the IEEE ComSoC Young Researcher Award in 2020. He was awarded an Alain Bensoussan Fellowship in 2012. He is the founder and EiC of *IET Journal of Quantum Communication*, vice chair of Europe/Africa Region—IEEE ComSoc: Green Communications Computing society and the IEEE Standard on P1932.1: Standard for Licensed/Unlicensed Spectrum Interoperability in Wireless Mobile Networks.

Keqin Li (Fellow, IEEE) is currently a SUNY distinguished professor of computer science with the State University of New York and the National distinguished professor with Hunan University, China. He has authored more than 870 journal articles, book chapters, and conference papers. His research interests include cloud computing, fog computing, mobile edge computing, and energy-efficient computing. Ranked among the top 5 most influential scientists in parallel and distributed computing based on Scopus citations, he is an associate editor for *ACM Computing Surveys* and *CCF Transactions on High Performance Computing*. He was also on the editorial boards of IEEE TRANSACTIONS ON PARALLEL AND DISTRIBUTED SYSTEMS and IEEE TRANSACTIONS ON COMPUTERS. He is a fellow of AAIA and a member of Academia Europaea.

Schahram Dustdar (Fellow, IEEE) received the PhD degree in business informatics from the University of Linz, Linz, Austria, in 1992. He has been the chairman of Informatics Section of the Academia Europaea, since 2016. He is currently a full professor of computer science (informatics) with a focus on internet technologies heading the Distributed Systems Group, TU Wien, Vienna, Austria. Prof. Dustdar was a member of the IEEE Conference Activities Committee. He has been a member of the Section Committee of Informatics of the Academia Europaea, since 2015, and the Academia Europaea: The Academy of Europe, Informatics Section, since 2013. He was the recipient of the ACM Distinguished Scientist Award in 2009 and the IBM Faculty Award in 2012. He is an associate editor for the IEEE TRANSACTIONS ON SERVICES COMPUTING, *ACM Transactions on the Web*, and *ACM Transactions on Internet Technology*. He is on the Editorial Board of multiple Transactions and journals of IEEE.